



### **Science Arts & Métiers (SAM)**

is an open access repository that collects the work of Arts et Métiers Institute of Technology researchers and makes it freely available over the web where possible.

This is an author-deposited version published in: <https://sam.ensam.eu>  
Handle ID: <http://hdl.handle.net/10985/8542>

#### **To cite this version :**

Philippe LE MASSON, Muriel CARIN, Morgan DAL - A model comparison to predict heat transfer during spot GTA welding - International Journal of Thermal Sciences - Vol. 75, p.54-64 - 2014

Any correspondence concerning this service should be sent to the repository

Administrator : [scienceouverte@ensam.eu](mailto:scienceouverte@ensam.eu)



# A model comparison to predict heat transfer during spot GTA welding

Morgan Dal, Philippe Le Masson\*, Muriel Carin

LIMATB, Université de Bretagne-Sud, UEB, centre de recherche C. Huygens, rue de Saint Maudé, 56321 Lorient cedex, France

## ABSTRACT

The present work deals with the estimation of the time evolution of the weld fusion boundary. This moving boundary is the result of a spot GTA welding process on a 316L stainless steel disk. The estimation is based on the iterative regularization method. Indeed, the three problems: direct, in variation and adjoint, classically associated with this method, are solved by the finite element method in a two-dimensional axisymmetric domain. The originality of this work is to treat an experimental estimation of a front motion using a model with a geometry including only the solid phase. In this model, the evolution of this solid domain during the fusion is set with the ALE moving mesh method (Arbitrary Lagrangian Eulerian). The numerical developments are realized with the commercial code COMSOL MULTIPHYSICS<sup>®</sup> coupled with the software MATLAB<sup>®</sup>. The estimation method has been validated in a previous work using theoretical data ([1]). The experimental data, used here for this identification are, temperatures measured by thermocouples in the solid phase, the temporal evolution of the melt pool boundary observed at the surface by a fast camera and the maximal dimensions of the melted zone measured on macrographs. These experimental data are also compared with numerical results obtained from a heat and fluid flow model taking into account surface tension effects, Lorentz forces and the deformation of the melt pool surface under arc pressure.

## Keywords:

TIG welding  
Multiphysics simulation  
Fluid flow  
Heat transfer  
Lorentz forces  
Marangoni effect  
Arbitrary Lagrangian Eulerian method  
Shape identification  
Iterative regularization method  
Adjoint problem  
Free boundary problem

## 1. Introduction

Due to its industrial applications, welding remains a particularly studied field. Implications of these studies involve the determination of operating parameters, the reduction of defects, and the control of residual stress and deformation. Two approaches can be encountered to meet these needs: an experimental one and a numerical one. The experimental approach requires many tests which consume a lot of time, money, and raw material. The numerical one requires a good understanding of all the physical phenomena occurring during the welding process.

In this paper, the numerical approach is applied to a Gas Tungsten Arc Welding (GTAW) process where the welding torch is fixed. The aim of this kind of study is generally to quantify the mechanical consequences of welding ([2,3]) but they are particularly dependent on the thermal field. Thus, in the present study, the main objective is to determine more accurately the temperature field. The temperature can be obtained from a multiphysics model. Tanaka et al. [4,5] have proposed a unified model taking into account the whole region of welding, namely, tungsten cathode, arc

plasma and weld pool. This approach requires high computational time. A more simple approach has been developed by a number of researchers (Kim et al. [6], Kumar and DebRoy [7,8], Mishra and DebRoy [9], Zhao et al. [10], Traidia et al. [11]). They have treated only the weld pool using a model coupling heat transfer, fluid flow and electromagnetism. However, the calculated predictions require distributions of heat flux and current density to be specified at the anode surface. The parameters of these distributions have to be quantified either from experimental investigations or from literature.

Another approach which consists in using equivalent heat source neglecting the fluid flow in the melt pool can be used. These studies, are usually built with equivalent heat sources avoiding the resolution of the fluid dynamic problem (Guo et al. [12] or Rouquette et al. [13]).

Both numerical methods have advantages and drawbacks. A multiphysics study needs large numerical resources and high computational time. A study with a simplified model (equivalent heat source for example) requires estimation of several parameters often linked to the energy input for a given welding case ([14–18]). The estimation is generally made using an inverse technique.

This paper presents both a multiphysics study and an inverse analysis. Our previous theoretical study [1] has been made to check the validity of a “reduced” model of the problem (based on the

\* Corresponding author.

E-mail address: philippe.le-masson@univ-ubs.fr (P. Le Masson).

## Nomenclature

$(r, z, \theta)$  coordinate system

### Roman

$a_i$	sulphur content
$\vec{B}$	magnetic induction field
$c_p$	specific heat
$D$	latent heat distribution function
$f_L$	liquid fraction
$\vec{g}$	gravity
$h_{cv}$	convective heat loss coefficient
$h_{tot}$	linear coefficient of heat losses
$I$	process current intensity
$\vec{j}$	current density
$J$	residual functional
$L_m$	latent heat of melting
$n$	measurement index
$N_c$	total number of measurements
$\vec{n}$	normal vector $p$ adjoint variable
$P$	pressure
$p_{arc}^{max}$	maximal arc pressure
$R$	maximal radius of the sample
$r_{th}$	standard deviation of the thermal Gaussian
$r_{elec}$	standard deviation of the electrical Gaussian
$s(r,t)$	estimated function
$t$	time
$t_{end}$	final time
$T(r,z,t)$	temperature field

$T_{fus}$	fusion temperature
$T_\infty$	ambient temperature
$T_{p,\infty}$	ambient wall temperature
$U$	process voltage
$\vec{V}(r,z,t)$	velocity field
$Y_n$	measured temperature
$Z$	maximal depth of the sample

### Greek

$\beta$	thermal expansion coefficient
$\delta(\dots)$	Dirac function
$\delta\theta$	variation of the dimensionless temperature
$\delta s$	variation of the estimated function (spatial variation)
$\Delta T$	mushy zone temperature range
$\epsilon$	dielectric permittivity of the material
$\varepsilon$	emissivity
$\gamma$	surface tension coefficient
$\eta$	thermal efficiency of the process
$\kappa$	curvature
$\lambda$	thermal conductivity
$\mu_L$	dynamic viscosity of the liquid
$\mu$	magnetic permeability of the material
$\theta$	dimensionless temperature
$\rho$	density
$\rho_L$	average of the density in the liquid phase
$\sigma$	Stefan–Boltzmann constant
$\sigma_{EM}$	electrical conductivity
$\sigma_\tau$	tangential strain
$\sigma_n$	normal strain

works of Doan et al. [19]) and the estimation method. In Refs. [1], a “simplified” simulation was compared to multiphysics simulation results. The maximal observed error was less than 2%. The present study is an application of this method in a real context, thus an experimental implementation is made. Nevertheless, the experimental data acquisition must be made carefully and theoretical study must be adjusted. The experimental data are also compared to a multiphysics model.

The context of the study is firstly presented. Then a heat and fluid flow multiphysics model is proposed. The numerical results are compared to experimental data such as thermal cycle, weld shape. After a brief explanation of the inverse method, the inverse study is applied to shape identifications. Finally, the predictions of multiphysics model and the moving fusion boundary model are compared.

## 2. Contexts

This study corresponds to GTA spot welding on a disk. This experimental simplification is used to reduce the size of the problem, because it leads to axisymmetric configuration. Thus, this simplified case makes it possible to focus on the transient phenomena which appear during the weld pool evolution. The melted zone expansion is studied during the first 20 s. Here, the sample is a 316L stainless steel disk (cylinder with diameter = 16 cm and depth = 1 cm – Fig. 1).

The main objective of the experimental part is the estimation of the front motion. Nevertheless, the experimental data are also used to validate the multiphysics simulation.

Table 1 gives the process parameter values. The last parameter corresponds to the starting method. In our case, since the process does not move, the arc is generated by the contact of the electrode onto the workpiece, followed by the withdrawal of the electrode.

## 3. Multiphysics study

In arc welding, the thermal field is the consequence of the interaction of many physical phenomena. Fig. 2 summarizes all the phenomena which directly affect the workpiece. This kind of multiphysics study is carried out in order to be predictive, which means that only the process parameters (current, voltage, ...) are used to obtain a reliable thermal field. In our case, the aim is the definition of a knowledge model.

### 3.1. The multiphysics model

The first assumption made to solve this problem refers to axial symmetry. Fig. 3 shows the geometry created for the simulation. Two main domains are defined ( $\Omega_1$  and  $\Omega_2$ ) in order to solve the

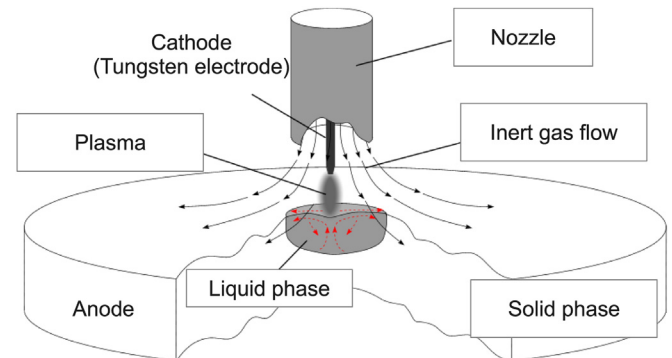


Fig. 1. Scheme of GTA spot welding on a disk.

**Table 1**  
GTAW process parameters.

Process parameters	Values	
$U$	10	V
$I$	150	A
Electrode diameter	2.4	mm
Electrode sharpening angle	45	°
Shielding gas	Ar > 99.998%	Arcal1 (Air Liquide)
Shielding gas flow rate	16	l min <sup>-1</sup>
Stick-out	10	mm
Arc length	1.2	mm
Starting method	Scraping	

mass and momentum conservation equations only, in the smaller volume ( $\Omega_1$ ), where the liquid appears, and to reduce calculation time. A second important assumption lies in the representation of the workpiece without simulating the arc plasma. Thus, the heat flux, the current density and the arc pressure which come from the plasma interaction (Fig. 2) are approximated by closed forms (Gaussian distributions with parameters deduced from the works of Tsai et al. [20,21] and those of Lin et al. [22,23]).

With regard to the **thermal problem**, the heat source induced by the Joule effect is neglected. The latent heat of the phase change is introduced in an equivalent heat capacity. The thermal properties of the material were gathered from the literature, and are temperature dependent [24].

For the **fluid flow** problem, the fluid is assumed to be Newtonian and incompressible. The flow is supposed to be laminar. Moreover, the Boussinesq approximations are used in order to allow buoyancy forces to be taken into account. The shear stress due to the shielding gas flow is assumed to be negligible compared to the thermocapillary forces induced by Marangoni effect. This effect is a consequence of active elements (sulphur, oxygen, ...) present in the material. In our case, the sulphur is assumed to be preponderant, and Sahoo's laws [25] can thus be applied:

$$\frac{\partial \gamma}{\partial T} = -A - R\Gamma_s \ln(1 + K_g a_i) - \frac{K_g a_i}{(1 + K_g a_i)} \frac{\Gamma_s \Delta H^0}{T} \quad (1)$$

$$K_g = k_i \exp\left(-\frac{\Delta H^0}{RT}\right) \quad (2)$$

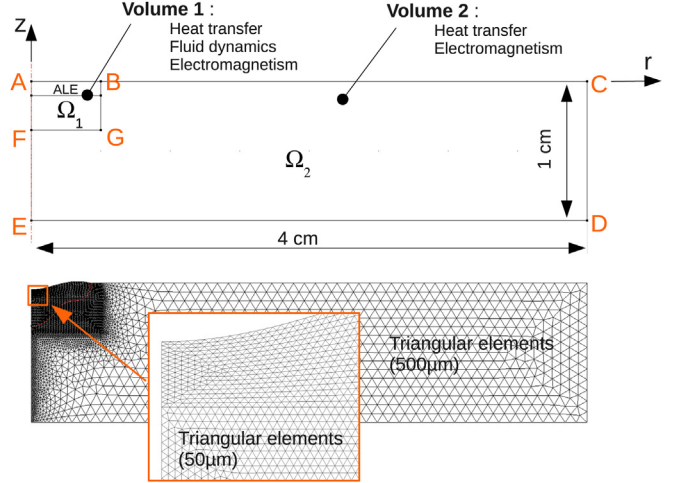


**Fig. 3.** Simulated geometry and mesh descriptions.

The parameter  $a_i$  is the sulphur content (wt%). Considering the results of Mishra et al. [9], which show a very fast homogenisation of the sulphur content, we have assumed that this content is initially homogeneous into the domain. Moreover, it should be noticed that in our case the quantity of sulphur is set by comparing experimental and numerical results (melt pool shape). Indeed, the Marangoni effect has a strong effect on the shape of the fusion zone. Thus, the sulphur content can be easily calibrated.

The last hypothesis concerns the flow inside the "mushy zone" which is assimilated to a porous media flow [26] and thus, approximated by the Darcy's law.

For the **electromagnetic problem**, the solved equations are written in magnetic field ( $\vec{B}$ ) and the electrical properties are chosen constants.

The link between these previous physics leads us to set many parameters (material properties, source properties, ...). Some of them can be found in the literature (material properties). Some others depend on our study, and the lack of knowledge leads us to assume them to be, for example, time independent.

The models, used in the simulation, are respectively, the energy conservation, the mass and momentum conservation and the Maxwell's equations.

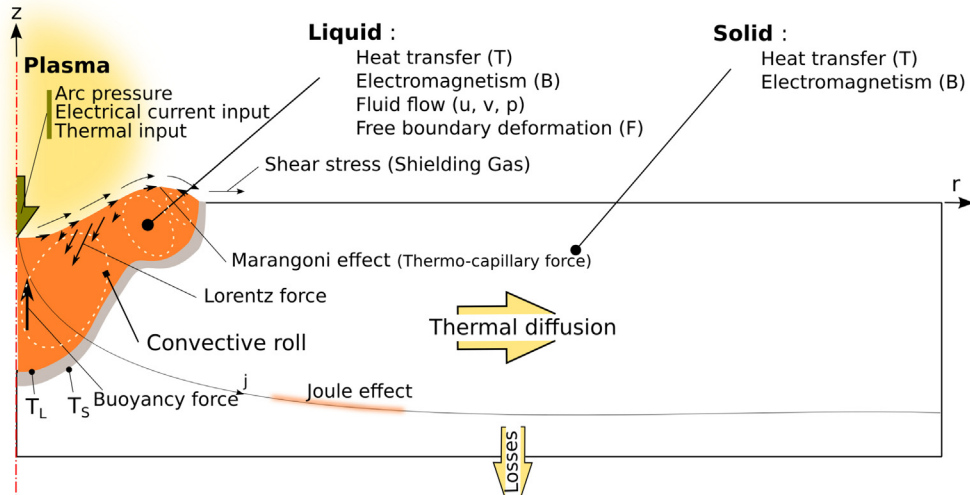


**Fig. 2.** Multiphysics couplings during welding.

### 3.1.1. The thermal problem

The thermal problem is governed by the classical energy conservation formulated in temperature (3) and where the latent heat of phase change is introduced into the bulk through a Gaussian distribution.

$$\rho(T)c_p(T)\left(\frac{\partial T}{\partial t} + u\frac{\partial T}{\partial r} + v\frac{\partial T}{\partial z}\right) = \frac{1}{r}\frac{\partial}{\partial r}\left(r\lambda(T)\frac{\partial T}{\partial r}\right) + \frac{\partial}{\partial z}\left(\lambda(T)\frac{\partial T}{\partial z}\right) + \rho L_m D(T)\frac{\partial T}{\partial t} \quad (3)$$

With  $D(T)$  the latent heat distribution factor,

$$D(T) = \frac{\partial f_l}{\partial T} \approx \frac{1}{\sqrt{\pi\Delta T^2}} \exp\left(-\frac{(T - T_{\text{fus}})^2}{\Delta T^2}\right) \quad (4)$$

The boundary conditions are written as:

$$[AB] \cup [BC] \rightarrow -\lambda(T)\frac{\partial T}{\partial n} = \frac{\eta UI}{2\pi r_{\text{th}}^2} e^{-\frac{r^2}{2r_{\text{th}}^2}} - h_{\text{cv}}(T - T_{\infty}) - \varepsilon\sigma(T^4 - T_{\text{p},\infty}^4) \quad (5)$$

$$[CD] \cup [DE] \rightarrow -\lambda(T)\frac{\partial T}{\partial n} = -h_{\text{cv}}(T - T_{\infty}) - \varepsilon\sigma(T^4 - T_{\text{p},\infty}^4) \quad (6)$$

$$[EF] \rightarrow -\lambda(T)\frac{\partial T}{\partial n} = 0 \quad (7)$$

In this equation system, the thermophysical properties are written in Table 2. Are presented, the thermal conductivity  $\lambda$ , the density  $\rho$ , the specific heat  $c_p$ , the viscosity of the liquid  $\mu_L$  or the latent heat  $L_m$ . In this table, some model parameters are presented as the convective heat transfer coefficient  $h_{\text{cv}}$  or the emissivity  $\varepsilon$ . Values of well known constants such as the Stefan–Boltzmann  $\sigma$  are not recall here.

### 3.1.2. The hydrodynamics and the free boundary problems

Considering the previously mentioned assumptions, the mass and momentum conservation equations can be written as:

$$\vec{\nabla} \cdot \vec{V} = 0 \quad (8)$$

With,

$$\rho_L \frac{\partial \vec{V}}{\partial t} + (\vec{V} \cdot \vec{\nabla}) \vec{V} = \vec{\nabla} \cdot \left( -P\mathbf{I} + \mu_L(T) (\vec{\nabla} \vec{V} + \vec{\nabla} \vec{V}^T) \right) + \dots + \underbrace{\vec{J} \wedge \vec{B}}_{\text{Lorentz}} + \underbrace{\frac{\mu_{L,\text{mean}}}{K} \vec{V}}_{\text{Darcy}} + \underbrace{\rho_L (1 - \beta(T - T_{\text{fus}})) \vec{g}}_{\text{Buoyancy}} \quad (9)$$

$$K = \frac{f_L^3}{c_l(1 - f_L)^2} \approx \frac{b + f_L^3}{c_l(1 - f_L)^2} \quad (10)$$

The boundary conditions applied on [AB] take into account surface tension, thermocapillary effect and arc pressure. They are composed of a tangential (11) and normal (12) terms:

**Table 2**

Numerical values used in the simulation.

Sources parameters	Values	
$U$	10	V
$I$	150	A
$p_{\text{arc}}^{\text{max}}$	900	N m <sup>-2</sup> [29]
$\eta$	68	%
$r_{\text{th}}$	$2 \times 10^{-3}$	m [20]
$r_{\text{elec}}$	$1.7 \times 10^{-3}$	m [20]
$r_{\text{pres}}$	$1.7 \times 10^{-3}$	m [30]
<i>Thermophysical properties</i>		
$\lambda(T)$		([24])
$\rho(T)$		([24])
$\rho_L$	6347	kg m <sup>-3</sup>
$c_p(T)$		([24])
$\mu_L(T)$		([31])
$L_m$	26,0000	J kg <sup>-1</sup>
$\beta$	$1.41 \times 10^{-5}$	K <sup>-1</sup> [32]
<i>Temperatures</i>		
$T_{\text{sol}}$	1658	K
$T_{\text{liq}}$	1723	K
$T(t_0)$	293	K
<i>Losses</i>		
$\varepsilon$	0.5	
$h_{\text{cv}}$	10	W m <sup>-2</sup> K <sup>-1</sup>
<i>Darcy law parameters</i>		
$c_l$	$7.3 \times 10^7$	
$b$	$1 \times 10^{-5}$	
<i>Electromagnetic properties</i>		
$\sigma_{\text{EM}}$	$1 \times 10^6$	S m <sup>-1</sup>
<i>Sahoo's law parameters [25]</i>		
$i$	Sulfur	
$k_l$	$3.18 \times 10^{-3}$	
$\Delta H^p$	$-1.66 \times 10^8$	J kg <sup>-1</sup> mol <sup>-1</sup>
$\Gamma_s$	$1.3 \times 10^{-8}$	kg mol m <sup>-2</sup>
$a_i$	0.0045	% <sub>m</sub>
$A$	$4.3 \times 10^{-4}$	N m <sup>-1</sup>
$T_{\text{fus}}$	1823	K

$$[AB] \rightarrow \sigma_{\tau} = -\mu_L \frac{\partial V_{\tau}}{\partial n} = \frac{\partial \gamma}{\partial T} \frac{\partial T}{\partial \tau} \quad (11)$$

$$[AB] \rightarrow \sigma_n = \gamma\kappa + \underbrace{p_{\text{arc}}^{\text{max}} e^{-\frac{r^2}{2r_{\text{th}}^2}}}_{P_{\text{arc}}} \quad (12)$$

$$[BG] \cup [GF] \rightarrow \vec{V} = \vec{0} \quad (13)$$

$$[FA] \rightarrow \vec{V} \cdot \vec{n} = 0 \quad (14)$$

The no slip condition (13) is chosen because the boundaries [BG] and [GF] remain a solid part. The last Eq. (14) represents the axial symmetry condition.

It should also be noticed that the motion of the free boundary is handled (from the fluid velocity) by the Arbitrary Lagrangian Eulerian method (ALE – [27]).

### 3.1.3. The electromagnetic problem

The formulation of the electromagnetic problem can be expressed in Azimuthal magnetic induction as follows (15) ([11] or [28]).

$$-\Delta B_\theta + \frac{B_\theta}{r^2} = -\mu\sigma_{EM}\frac{\partial B_\theta}{\partial t} - \varepsilon\mu\frac{\partial^2 B_\theta}{\partial t^2} \quad (15)$$

where the parameters  $\mu$  and  $\varepsilon$  are, respectively the magnetic permeability and the dielectric permittivity.

In this problem, the boundary conditions are more understandable in current density, thus both formulations are written here.

$$j_z = \frac{I}{2\pi r_{elec}^2} e^{-\frac{r^2}{2r_{elec}^2}} \rightarrow B_\theta + r \frac{\partial B_\theta}{\partial r} = r\mu \frac{I}{2\pi r_{elec}^2} e^{-\frac{r^2}{2r_{elec}^2}} \quad (16)$$

$$j_z = 0 \rightarrow B_\theta + r \frac{\partial B_\theta}{\partial r} = 0 \quad (17)$$

$$j_r = 0 \rightarrow \frac{\partial B_\theta}{\partial z} = 0 \quad (18)$$

In the present work, Eq. (15) is solved using a transient solver. However, it should be noticed that the characteristic time of this electromagnetic problem ( $1.10^{-5}$  s to reach the stationary state) is much smaller than the one of the diffusive problem. So, in many works, the problem is reduced to a magneto-static model.

### 3.2. Material properties

The whole parameters used in the simulation are summarized in Table 2. Some of them have been measured during experiment ( $U$ ,  $I$ ), others are estimated with a sensitivity analysis ( $r_{th}$ ,  $r_{elec}$ ,  $r_{pres}$ ,  $a_i$ ) and the lasts are taken from the literature ( $\lambda$ ,  $\rho$ ,  $c_p$ ,  $L_m$ , ...).

The evolution of thermal properties ( $\lambda(T)$ ,  $\rho(T)$ ,  $c_p(T)$  and  $\mu_L(T)$ ) with temperature are shown in Appendix.

### 3.3. Numerical scheme

In order to understand the high computational time needed to solve the problem some details must be pointed out.

The partial differential equations are solved with the commercial software COMSOL MULTIPHYSICS® v3.5a which uses the finite element method. The fully coupled resolution has been performed with the parallel sparse direct linear solver PARDISO. The numerical scheme used to solve the time-dependent problem is the implicit generalized-alpha method. An adaptative time-stepping is used with a maximum time step of 0.001 s. The error is controlled with an absolute tolerance of 0.01 (with the unit of each calculated variable) and a relative tolerance of 0.01%.

The mathematical equations of the multiphysics problem are discretized in quadratic elements for the thermal problem and for the velocity field, in linear elements for the pressure, and in cubic elements for the electromagnetic problem (to avoid numerical oscillations). The ALE method is used to treat the motion of the free boundary. The interpolation on geometric elements is quadratic and we have used a Winslow smooth method. Thus, the model consists in 250,000 degrees of freedom which are solved in approximately three days. The used computer has 8 CPU at 3.33 GHz and with 600 MHz for the random access memory.

### 3.4. Numerical results

Fig. 4 presents the melt pool shapes, the thermal field and velocity field vector at different times. Some isothermal lines are added

to illustrate the convective effect on the thermal field. The temperature scale shows a maximal value of 2314 K, located at the top face of the sample and on the symmetry axis. This high temperature level is the result of the Gaussian heat source which represents the arc energy input. This heat is convected at the outer edge of the weld pool due to the Marangoni effect. Indeed, due to the thermocapillary forces, two opposite flow (one the free boundary) are induced. The resulting flow moves towards the bottom of the melt pool and generates the convective cell observed at the periphery. The particular shape of the melt pool is thus the result of active element concentration (sulphur).

To check the reliability of this numerical results, an experimental investigation is performed. The temperatures and fusion zone shapes are compared. However, the velocities in the melt pool have not been measured. Nevertheless, our calculated values are consistent with the published numerical works performed on GTA spot welding. For example, Tanaka et al. [5] have found a maximal value of  $0.66 \text{ m s}^{-1}$  and Oreper et al. [33] have reported a value of  $0.64 \text{ m s}^{-1}$ . Thus, our value of  $0.5 \text{ m s}^{-1}$  is consistent with these observations. The discrepancy comes from the Marangoni effect, which is temperature-dependent in our study and which tends to reduce the radial velocity.

## 4. Experimental validation

The experiment is the application of the GTAW process on a 316L sample (the workpiece). In order to have as much information as possible, five “spots” are made: three cases with a process applied during 20 s and two during 9 s. For each case, the temperature is measured by thermocouples (K type). Nine thermocouples are introduced into the sample nearby the maximal location of the fusion front. In this experiment, they have a diameter of  $50 \text{ }\mu\text{m}$  which leads to hot junctions of around  $210 \text{ }\mu\text{m}$  in diameter. Thus, the measurement system has a very small thermal inertia and since the thermocouples are welded at the bottom of holes, we can assume both a satisfactory observation of fast variations of the temperature and an accurate measurement of the temperature. The holes have a diameter of  $650 \text{ }\mu\text{m}$  and they are drilled from rear face of the sample. The temperatures are acquired with a frequency of 100 Hz.

The motion of the front is observed on the surface with a fast camera Phantom V5 ( $f = 100 \text{ Hz}$  and  $512 \times 512$  pixels), and the maximal shape of the fusion zone is measured on macrographs.

The use of thermocouples allows a good measurement of temperature up to  $1000 \text{ }^\circ\text{C}$  (Fig. 5). In this figure, at the bottom right, the location of the sensors is illustrated. The thermocouples are about 1 mm distant from the melt pool boundary.

The comparison, illustrated in Fig. 5, shows a too slow rise of the simulated temperature during the very first seconds. This can be interpreted as a too slow growing of the fusion zone. Nevertheless, the temperatures simulated at the ending time are very close to the measurements. It should be noticed that in Fig. 5, the measured temperatures are corrected from the error model presented at the end of Section 5.

The results shown in Figs. 6 and 7 come from fast camera videos and macrographs. For the first one, the difficulty comes from the saturation due to the arc plasma. The use of an optical filter and halogen lights makes it possible to measure with satisfactory accuracy ( $\pm 1 \text{ pixel} \approx 0.07 \text{ mm}$ ). For the second, the difficulty lies in the formulation of an acid that could corrode a stainless steel, here we have used “Aqua regia”. For this measurement, the difficulty is the temperature knowledge of the boundary observed on macrographs. We assume this front at the solidus temperature.

The comparison of the surface front motion (Fig. 6) shows that the simulated front is slower than the experimental one during the first



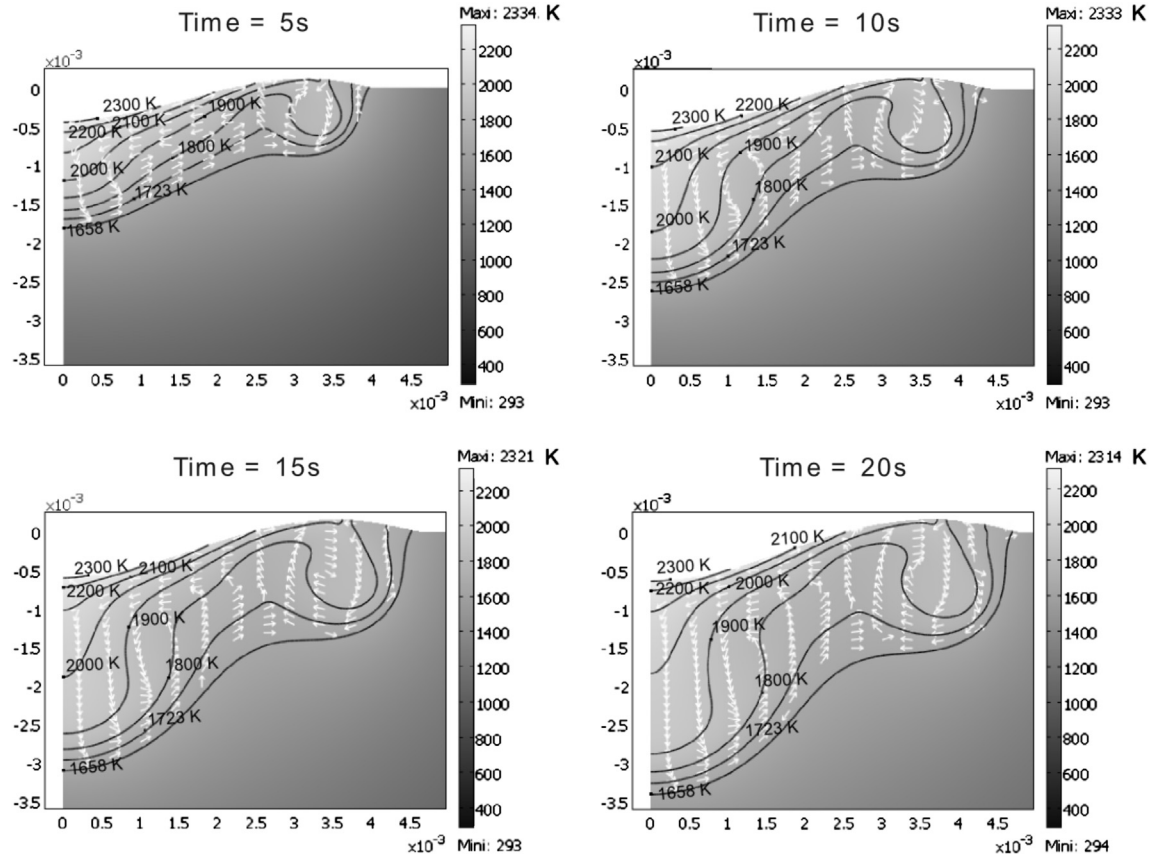


Fig. 4. Multiphysics results – evolution of the weld pool shape, thermal field, velocity vector field and isothermal lines.

6 s. Then, the simulation gives results very close to the experiment. This experiment demonstrates also the axisymmetry of the melt pool.

Fig. 7 shows a comparison between the measured and the simulated fusion zones. In order to have a transient validation, the shapes are compared at  $t = 9$  s and  $t = 20$  s. In both cases, the differences are quite similar: the model predicts a smaller penetration and a slightly higher width. Nevertheless, the width of the simulated weld pool is very close to the experimental one.

The first results of this simulation are quite satisfactory but, as shown in Figs. 5–7, the differences between the measurements and the simulations are time-dependent. This seems to be the consequence of using steady sources in a time-dependent analysis. It should be interesting to estimate this time evolution, but the high number of unknown parameters and the calculation duration do

not allow the use of inverse methods. Thus, the problem is considered differently, by using inverse methods for the estimation of the front motion into a simplified model.

## 5. Inverse analysis

As previously mentioned, the computational time of the multiphysics problem is very long, and many parameters have to be set (Gaussian distributions, arc efficiency, sulphur concentration, ...).

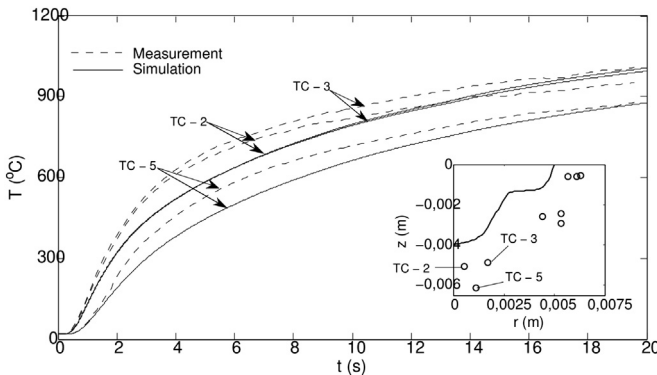


Fig. 5. Comparison between measured and simulated temperatures for three thermocouples.

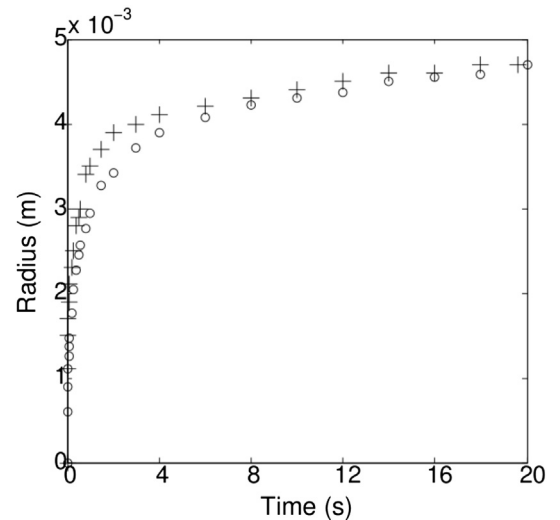


Fig. 6. Comparison between the simulated and measured width of the melt pool (cross marks and circles represent respectively measurements and simulated results).

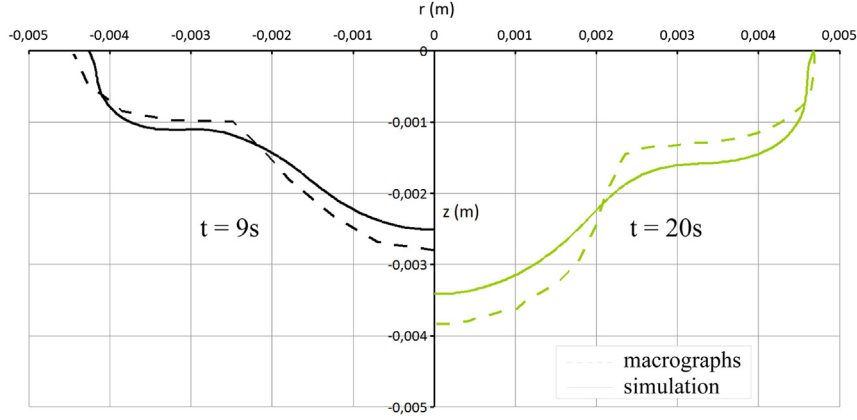


Fig. 7. Comparison between measured and simulated shapes of the weld pool for two times (9 s and 20 s).

Moreover, the discrepancy between the multiphysics study and experimental results needs to be analysed.

The temperature into the solid phase is the main relevant information to quantify the mechanical consequences. Thus, our intention is to reduce the size of the model and to deal solely with the conductive heat transfers in the solid part (Fig. 8).

In this problem, the fusion front is the source of the heat transfers in the solid phase. It cannot be directly observed or measured, and the most efficient tools, to get this information, are the inverse methods.

This simulation method is based on previous works [1]. To avoid the simulation of the liquid part, the locations and the temperature ( $T_{sol}$ ) of the fusion front are set. This reduces the computational time from 72 h with the multiphysics model to only 10 min with the reduced problem.

To do this, the numerical domain is modified with the Arbitrary Lagrangian Eulerian method and the motion of the front is prescribed as a displacement of a moving boundary (Fig. 9). The particularity of this “solid phase” simulation is the knowledge of the front location at each time step. Indeed, in a classical analysis the front motion is the result of the simulation. In our case, the front locations are prescribed for all time steps. Thus, the inverse analysis has been applied to estimate them. In other words, we have to estimate functions ([13]) containing the coordinates of the curve ([AB] in Fig. 9) representing the front (one curve for each time step). An iterative regularization method is used [34]. A theoretical application has already been validated [1]. This method allows the reduction of a quadratic criterion (Eq. (19)) built on the measured and simulated temperatures (equation system (20)–(26)) difference.

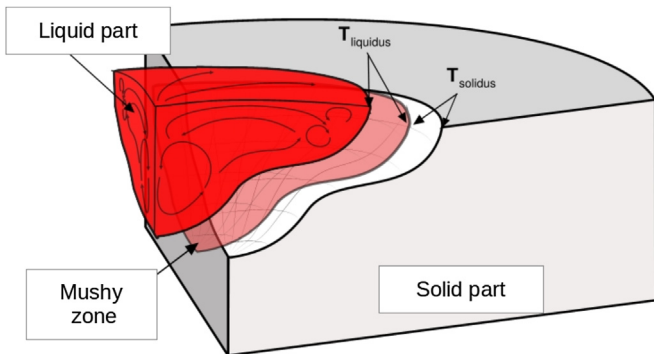


Fig. 8. Computational configuration for the simplified model.

$$J(s) = \frac{1}{2} \sum_{n=1}^{N_c} \frac{r_n}{R} \left( \int_0^{t_{\text{end}}} [\theta(r_n, z_n, t; s) - \tilde{Y}_n(t)]^2 dt \right) \quad (19)$$

In this criterion, the sum of quadratic differences is made on each measurement points (from 1 to  $N_c$  the number of thermocouples). The difference is factorised by the ratio of the measurement locations by the total length of the sample to avoid difficulties during the formulation of the adjoint problem. As shown in Eq. (35), the  $r_n$  is simplified. This factor has no influence on the criterion reduction.

### 5.1. Equation systems

The resolutions of equation systems written in the three next parts are performed with the commercial software COMSOL MULTIPHYSICS®.

#### 5.1.1. Direct problem

The direct problem is a classical energy conservation equation (Eq. (20)) with Dirichlet (Eq. (21)) and Neumann boundary conditions (Eqs. (22)–(25)).

$$\rho(\theta) c_p(\theta) \frac{\partial \theta}{\partial t} = \frac{1}{r} \frac{\partial}{\partial r} \left( \lambda(\theta) r \frac{\partial \theta}{\partial r} \right) + \frac{\partial}{\partial z} \left( \lambda(\theta) \frac{\partial \theta}{\partial z} \right) \quad (20)$$

$$[AB] \quad \theta(r, s, t) = 0 \quad (21)$$

$$[BC] \cup [CD] \quad -\lambda(\theta) \frac{\partial \theta(r, z, t)}{\partial z} = \frac{-S(r)}{(T_{\text{fus}} - T_{\infty})} + h_{\text{tot}}(\theta(r, z, t) + 1) \quad (22)$$

$$[DE] \quad -\lambda(\theta) \frac{\partial \theta(r, z, t)}{\partial r} = h_{\text{tot}}(\theta(r, z, t) + 1) \quad (23)$$

$$[EF] \quad \lambda(\theta) \frac{\partial \theta(r, z, t)}{\partial z} = h_{\text{tot}}(\theta(r, z, t) + 1) \quad (24)$$

$$[FA] \quad \lambda(\theta) \frac{\partial \theta(r, z, t)}{\partial r} = 0 \quad (25)$$

$$\text{for } t = 0 \quad \theta(r, z, t) = -1 \quad (26)$$

It should be noted that the solved variable is not really the temperature ( $T$ ) but a dimensionless temperature ( $\theta = (T - T_{\text{sol}})/(T_{\text{sol}} - T_{\infty})$ ). The Eq. (21) corresponds to the fusion temperature prescribed at the moving front. The heat source  $S(r)$  is a part of a Gaussian law designed to avoid heat flux discontinuity and thus to



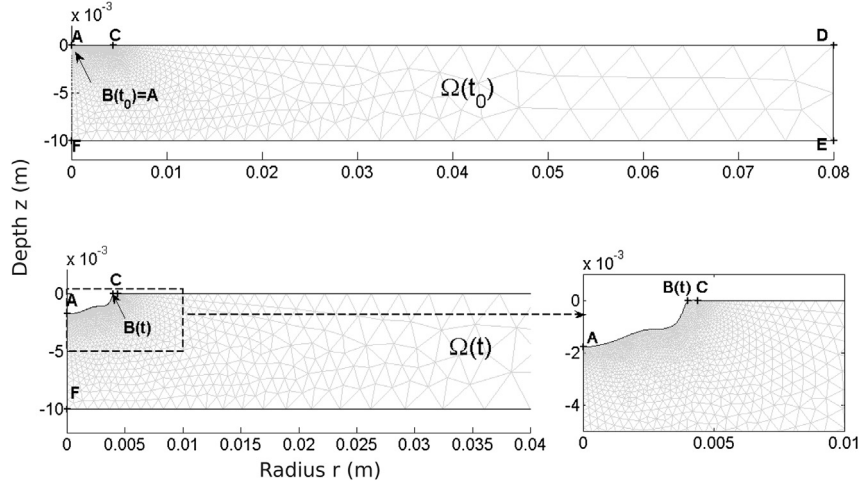


Fig. 9. Front tracking principle – name of vertexes.

avoid the rise of a numerical heat flux perturbing the temperature calculation.  $h_{\text{tot}}$  is a linearised convective coefficient.

### 5.1.2. Sensitivity problem

The sensitivity problem is developed for the calculation of the descent step. The resolution of this problem shows the effect of the unknown functions ( $\delta s$  front shapes) variation on the thermal field ( $\delta \theta$ ).

The equation system is formulated as a classical diffusive problem (Eq. (27)) with Neumann conditions (Eqs. (29)–(32)).

$$\frac{\partial(\rho(\theta)c_p(\theta)\delta\theta)}{\partial t} = \frac{1}{r} \frac{\partial}{\partial r} \left( r \frac{\partial(\lambda(\theta)\delta\theta)}{\partial r} \right) + \frac{\partial^2(\lambda(\theta)\delta\theta)}{\partial z^2} \quad (27)$$

$$[AB] \quad \delta\theta(r, s, t) = \delta s \frac{\partial\theta}{\partial z} \quad (28)$$

$$[BC] \cup [CD] \quad - \frac{\partial(\lambda(\theta)\delta\theta)}{\partial z} = h_{\text{tot}}\delta\theta \quad (29)$$

$$[DE] \quad - \frac{\partial(\lambda(\theta)\delta\theta)}{\partial r} = h_{\text{tot}}\delta\theta \quad (30)$$

$$[EF] \quad \frac{\partial(\lambda(\theta)\delta\theta)}{\partial z} = h_{\text{tot}}\delta\theta \quad (31)$$

$$[FA] \quad \frac{\partial(\lambda(\theta)\delta\theta)}{\partial r} = 0 \quad (32)$$

$$\text{for } t = 0 \quad \delta\theta = 0 \quad (33)$$

Only the condition on [AB] is not classical. On this boundary at constant temperature, we assume that a shape variation ( $\delta s$ ) can be assimilated to a temperature variation ( $\delta\theta$ ). Thus, the solicitation is formulated as (28) [34].

### 5.1.3. Adjoint problem

The adjoint problem allows the calculation of the descent direction. More details are presented in a previously published work [1]. Moreover, these equations are the result of the Lagrangian variational formulation.

With several developments and a factorization by  $r$ , the adjoint equation can be written as follows:

$$-\rho(\theta)c_p(\theta) \frac{\partial p}{\partial t} = \lambda(\theta) \frac{\partial}{\partial r} \left( r \frac{\partial p}{\partial r} \right) + \lambda(\theta) \frac{\partial^2 p}{\partial z^2} + S(r, z, t) \quad (34)$$

With :

$$S(r, z, t) = \frac{1}{R} \sum_{n=1}^{N_c} [\theta(r, z, t; s) - \tilde{Y}(t)] \delta(r - r_n) \delta(z - z_n) \quad (35)$$

$$[AB] \quad p(r, s, t) = 0 \quad (36)$$

$$[BC] \cup [CD] \quad - \lambda(\theta) \frac{\partial p}{\partial z}(r, z_0, t) = h_{\text{tot}} p(r, z_0, t) \quad (37)$$

$$[DE] \quad - \lambda(\theta) \frac{\partial p}{\partial r}(R, z, t) = h_{\text{tot}} p(R, z, t) \quad (38)$$

$$[EF] \quad \lambda(\theta) \frac{\partial p}{\partial z}(r, Z, t) = h_{\text{tot}} p(r, Z, t) \quad (39)$$

$$[FA] \quad \lambda(\theta) \frac{\partial p}{\partial r}(r_0, z, t) = 0 \quad (40)$$

$$\text{for } t = t_{\text{end}} \quad p(r, z, t_{\text{end}}) = 0 \quad (41)$$

$\theta(r, z, t; s)$  and  $\tilde{Y}(t)$  are respectively, the simulated and measured dimensionless temperature, thus the source  $S(r, z, t)$  of the adjoint problem is built from the discrepancy between model and experiment. The time condition of this problem is the solution at the last time step (41). Therefore, the system needs a backward resolution.

To minimize  $J(s)$ , we have previously shown [35] that three kinds of information are necessary to correctly estimate the location of the front at different times:

- The temperature, measured at different locations in the solid phase (Fig. 5).
- The surface front motion, extracted from fast camera videos (Fig. 6).
- The shape of the front at the last time step, observed on macrographs (Fig. 7).

### 5.2. Inverse results

Fig. 10A–C shows the evolution of the front shapes. In these three figures, the vertical axis ( $z$ ) is the depth of the fusion zone, the horizontal one – named  $r$  – is the radius, and the one named  $t$  is the time. Thus, these pictures give a representation of the motion of the

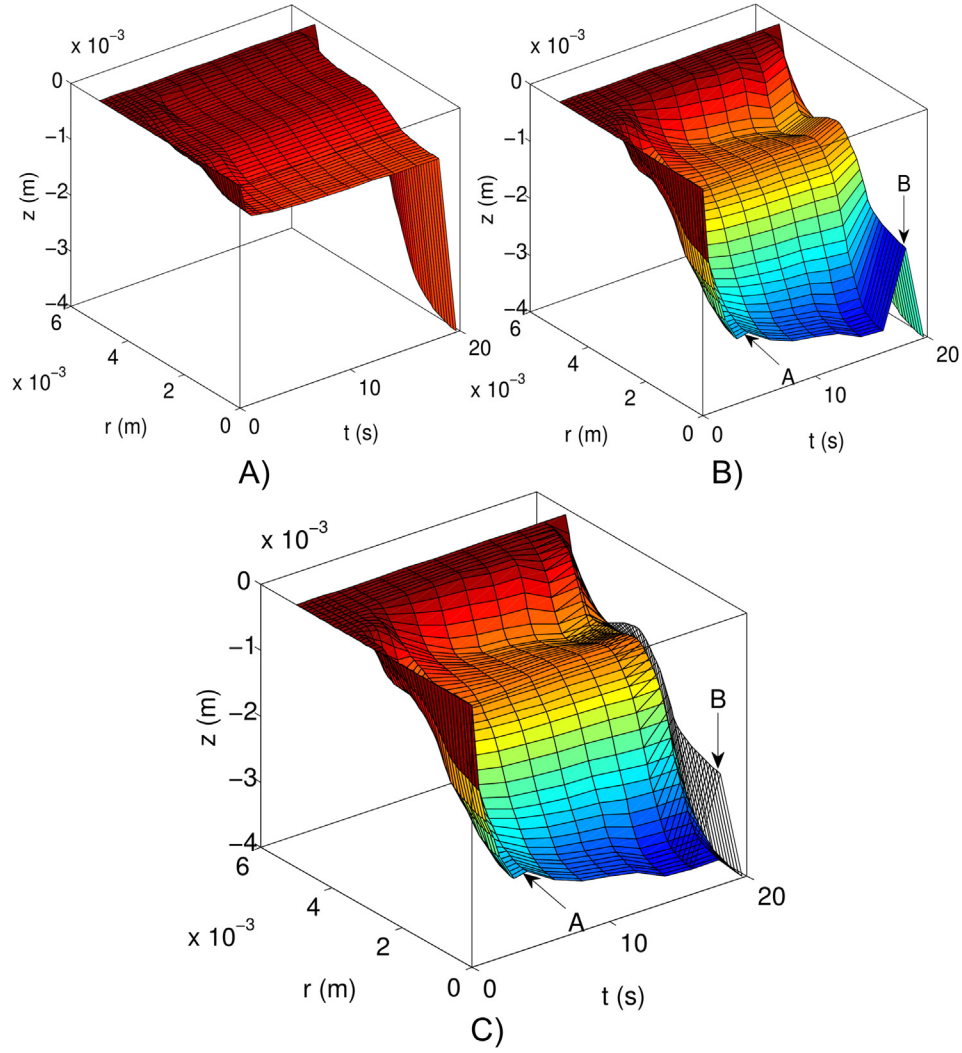


**Fig. 10.** Tri-dimensional representation of the results – A) Initial guess, B) results after estimation and C) results after corrections.

front: no fusion zone on the left (for  $t = 0$ ) and the macrograph measurements on the right (for  $t = 20$  s).

Fig. 10A presents the initial guess for the estimation. The curve representing the front shape at  $t = 20$  s is directly set at the true value because this information is measured. The surface evolution

is also directly imposed using the fast camera videos. However, the initial choice of the front space distributions is arbitrary.

Fig. 10B is a tri-dimensional representation of the front motion after the identification procedure. At this step, the residual value is equivalent to a standard deviation equal to  $35^\circ\text{C}$ . Two singularities

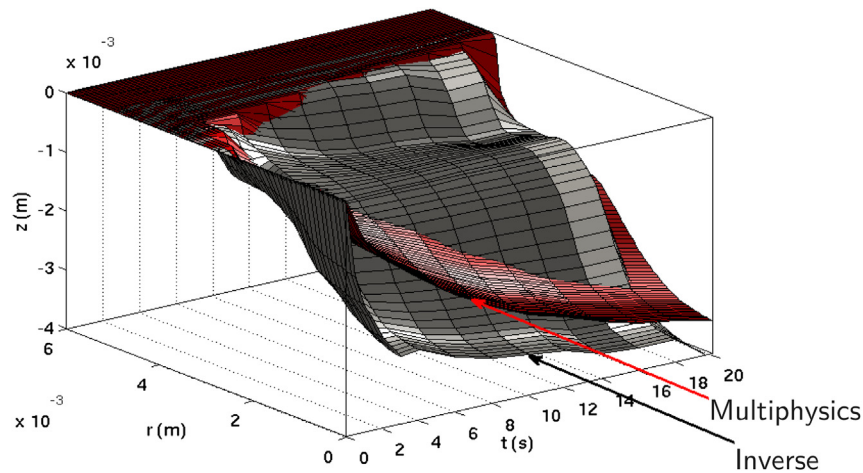


**Fig. 11.** Comparison between inverse and multiphysics front locations.

are pointed out (A and B) and both are local rises in the front location. The first (A) occurs at  $t = 4$  s and the second (B) at  $t = 18$  s. The analysis of this result needs the consideration of the classical errors founded in this kind of problems. These errors are clearly defined in Ref. [36], but we assume that only two of them have a significant effect on the estimated results:

- The **ability of parameters to be estimated** with the selected inverse method. Here the problem comes from the inverse method that is used. Indeed, the adjoint variable,  $p$ , allows for the determination of the descent direction, and  $p$  is equal to zero at the last time step,  $t_{\text{end}}$ . Thus, the descent is also close to zero for times near  $t_{\text{end}}$  and this is the reason for the important error illustrated by the B point of Fig. 10B. Here, a correction can be easily applied by imposing, at  $t = 18$  s, the shape of the front estimated at  $t = 16$  s (Fig. 10C).
- The **bias generated by the sensor itself**. Indeed, the thermal diffusion is affected by the hole drilled to insert the thermocouple. The heat flux cannot go through the air and an accumulation is observed near the sensor. Thus, the measured temperature is higher than the actual one (up to 80 °C [1]). Here, the correction is more complex. A tri-dimensional simulation is developed to take the sensor geometry into account. A comparison between the temperature inside the thermocouple and the temperature on an unaffected zone leads to a maximal error. This error is then directly corrected on measured temperatures, and the criterion is automatically reduced (standard deviation  $\approx 30$  °C). The resolution of the inverse problem with a model that takes the sensors into account should be the better solution to avoid biases, but this kind of resolution is too costly in calculation time.

## 6. Result comparisons between multiphysics and inverse analysis

A comparison between the results obtained from both methods is therefore interesting in order to detect gaps in the considered physical phenomena. In this sense, the information which can be observed is the front locations (Fig. 11).

Fig. 11 shows the result in terms of front shapes for both methods. The inverse results are considered as the most reliable because of the good adequation between measured and simulated temperatures (small value of the criterion). The front evolution which is observed for the multi-physics simulation is slower than the one coming from the inverse problem. This is the origin of the slow evolution of the temperature observed in Fig. 5.

Fig. 11 shows a good adequation of the front motion at the surface of the fusion zone ( $z = 0$ ) calculated with the multiphysics model, as compared to the one obtained through the inverse method. Both methods tend to give similar front shapes at the last time step, and both allow for a realistic representation of the convective cell effect (at the periphery) in the melt pool.

In this figure, the important observation is the one that deals with the transient aspect of the weld pool generation. In fact, the shape evolutions calculated by the multiphysics simulation is very slow compared to the inverse results (Fig. 11). This is a consequence of the arc efficiency which is assumed to remain constant during process. This classical assumption neglects the dynamics of the generation and stabilization of the arc plasma. But here, we have shown that this hypothesis is not suitable when dealing with a transient case of welding.

## 7. Conclusion

This study is based on previous theoretical work which consisted of a validation of the inverse method that is used here. In

parallel with this inverse analysis, a multiphysics simulation has been developed in order to take into account the heat transfers, the fluid flow, the electromagnetism, and the deformation of the melt pool surface. The most relevant results have been compared to those coming from estimations.

The application of the inverse method to experimental data implies meeting with some classical difficulties, such as the disturbance caused by the sensor, or the effect of the adjoint problem on the criterion reduction. The simulation of the sensor in the geometry is not feasible, some suggestions are thus made to overcome these problems and to correct the solutions.

Obviously, the aims of each method are not really the same, but comparing them leads to very interesting observations. Indeed, the estimated front motion illustrates a very fast evolution during the first seconds. This evolution is not correctly obtained through the multiphysics simulation. In fact, it is the energy input, assumed to be constant in time, which is the origin of this error. In future work, it could be interesting to identify this time evolution of the energy input through the definition of a time-dependent efficiency  $\eta(t)$  or time-dependent radial distribution  $r_{\text{th}}(t)$ .

## Acknowledgements

The authors are very grateful to the “Université Européenne de Bretagne”, to the region of “Bretagne”, to the “Laboratoire de Mécanique et Génie Civil” of the “Université Montpellier 2” and to the AREVA group.

## Annexe A. Thermal properties

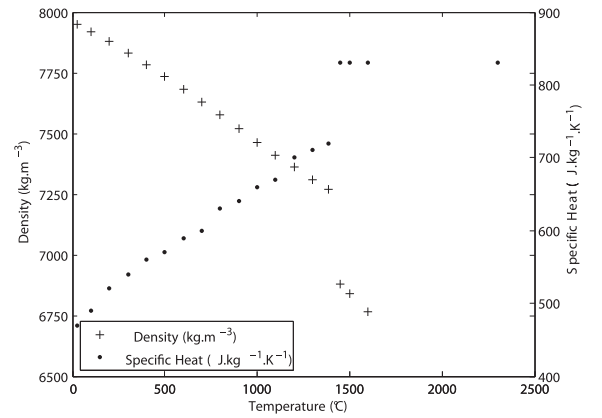


Figure A.12. Density and specific heat used in the simulations.

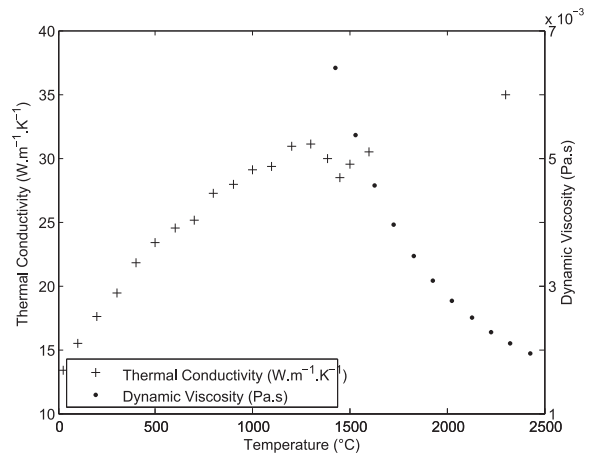


Figure A.13. Thermal conductivity and viscosity used in the simulations.

## References

- [1] M. Dal, P. Le Masson, M. Carin, Estimation of fusion front in 2d axisymmetric welding using inverse method, *International Journal of Thermal Science* 55 (2012) 60–68.
- [2] X. Shan, C.M. Davies, T. Wangsdan, N.P. O'Dowd, K.M. Nikbin, *International journal of pressure vessels and piping*, *International Journal of Pressure Vessels and Piping* 86 (2009) 110–121.
- [3] N. Kerrouault, *Fissuration à chaud en soudage d'un acier inoxydable austénitique* (Ph.D. thesis), Ecole Centrale Paris, 2001.
- [4] M. Tanaka, H. Terasaki, M. Ushio, J.J. Lowke, A unified numerical modeling of stationary tungsten-inert-gas welding process, *Metallurgical and Materials Transactions A* 33A (2002) 2043–2052.
- [5] M. Tanaka, M. Ushio, J. Lowke, Numerical analysis for weld formation using a free-burning helium arc at atmospheric pressure, *JSME International Journal Series B* 48 (3) (2005) 397–404.
- [6] W.H. Kim, S.J. Na, Heat and fluid flow in pulsed current GTA weld pool, *International Journal of Heat and Mass Transfer* 41 (1998) 3213–3227.
- [7] A. Kumar, T. DebRoy, Calculation of three-dimensional electromagnetic force field during arc welding, *Journal of Applied Physics* 94 (2) (2003) 1267–1277.
- [8] A. Kumar, T. DebRoy, Heat transfer and fluid flow during gas-metal-arc fillet welding for various joint configurations and welding positions, *Metallurgical and Materials Transactions A* 38A (2007) 506–519.
- [9] S. Mishra, T.J. Lienert, M.Q. Johnson, T. DebRoy, An experimental and theoretical study of gas tungsten arc welding of stainless steel plates with different sulfur concentrations, *Acta Materialia* 56 (2008) 2133–2146.
- [10] P.C. Zhao, C.S. Wu, Y.M. Zhang, Numerical simulation of the dynamic characteristics of weld pool geometry with step-changes of welding parameters, *Modelling and Simulation in Materials Science and Engineering* 12 (2004) 765–780 (2004) 765–780.
- [11] A. Traidia, F. Roger, E. Guyot, Optimal parameters for pulsed gas tungsten arc welding in partially and fully penetrated weld pools, *International Journal of Thermal Sciences* 49 (2010) 1197–1208.
- [12] J. Guo, P. Le Masson, E. Artioukhine, T. Loulou, P. Rogeon, D. Carron, M. Dumons, J. Costa, Estimation of a source term in a two dimensional heat transfer problem: application to an electron beam welding, in: 4th International Conference on Inverse Problems: Identification, Design and Control, Moscow, Russia, 2003.
- [13] S. Rouquette, J. Guo, P. Le Masson, Estimation of the parameters of a Gaussian heat source by the Levenberg–Marquardt method: application to the electron beam welding, *International Journal of Thermal Sciences* 46 (2007) 128–138, 46 (2007) 128–138.
- [14] S. Bag, A. Trivedi, A. De, Use of a multivariate optimization algorithm to develop a self-consistent numerical heat transfer model for laser spot welding, *International Journal of Advanced Manufacturing Technology* 38 (2008) 575–585.
- [15] C.V. Goncalves, L.O. Vilarinho, A. Scotti, G. Guimaraes, Estimation of heat source and thermal efficiency in GTAW process by using inverse techniques, *Journal of Materials Processing Technology* 172 (2006) 42–51.
- [16] A. Kumar, T. DebRoy, Guaranteed fillet weld geometry from heat transfer model and multivariable optimization, *International Journal of Heat and Mass Transfer* 47 (2004) 5793–5806.
- [17] D.D. Doan, *Modèle de source de chaleur pour la simulation du soudage avec et sans apport de matière* (Ph.D. thesis), Ecole Polytech'Nantes, 2006.
- [18] S. Mishra, T. DebRoy, Tailoring gas tungsten arc weld geometry using a genetic algorithm and a neural network trained with convective heat flow calculations, *Materials Science and Engineering A* 454–455 (2007) 477–486.
- [19] D. Doan, F. Gabriel, Y. Jarny, P. Le Masson, Weld pool shape identification by using Bezier surfaces, *Heat Transfer Engineering* 32 (2011) 771–786.
- [20] N. Tsai, *Heat Distribution and Weld Bead Geometry in Arc Weld* (Ph.D. thesis), Massachusetts Institute of Technology, 1983.
- [21] N.S. Tsai, T.W. Eagar, Distribution of the heat and current fluxes in gas tungsten arcs, *Metallurgical Transactions A* 16B (1985) 841–846.
- [22] M.L. Lin, T.W. Eagar, Influence of surface depression and convection on arc weld pool geometry, *Transport Phenomena in Materials Processing*, ASME PED 10 (1983) 63–69.
- [23] M.L. Lin, T.W. Eagar, Influence of arc pressure on weld pool geometry: a new model of a compound vortex is proposed as a possible mechanism to explain the deep surface depression encountered at currents over 300 amperes, *Welding Research Supplements*.
- [24] K.C. Mills, *Recommended Values of Thermophysical Properties for Selected Commercial Alloys*, Chandos Publishing, 2002.
- [25] P. Sahoo, T. DebRoy, M.J. McNallan, Surface tension of binary metal-surface active solute systems under conditions relevant to welding metallurgy, *Metallurgical Transactions B* 19B (1988) 483–491.
- [26] P.C. Carman, Fluid flow through granular beds, *Transactions of the Institution of Chemical Engineers* 75 (1997) s32–s48, Jubilee Supplement.
- [27] C.W. Hirt, A.A. Amsden, J.L. Cook, An arbitrary Lagrangian–Eulerian computing method for all flow speeds, *Journal of Computational Physics* 135 (1997) 203–216.
- [28] K.B. Bisen, M. Arenas, N. El-Kaddah, V.L. Acoff, Computation and validation of weld pool dimensions and temperature profiles for gamma TiAl, *Metallurgical and Materials Transactions A* 34A (2003) 2273–2279.
- [29] D. Fan, M. Ushio, F. Matsuda, Numerical computation of arc pressure distribution, *Transaction of JWRI* 15 (1986) 1–5.
- [30] M.L. Lin, T.W. Eagar, Pressures produced by gas tungsten arcs, *Metallurgical Transactions B* 17B (1986) 601–607.
- [31] C.S. Kim, *Thermophysical Properties of Stainless Steels*. Tech. rep, Argonne National Lab. III, USA, 1975.
- [32] M. Brochard, *Modèle couplé cathode-plasma-pièce en vue de la simulation du procédé de soudage à l'arc tig* (Ph.D. thesis), Université de Provence, 2009.
- [33] G.M. Oreper, T.W. Eagar, J. Szekeely, Convection in arc weld pools: electromagnetic and surface tension forces are shown to dominate flow behavior, in some cases producing double circulation loops in the weld pool, *Welding Research Supplement* (1983) 307–312.
- [34] C.-H. Huang, M.-T. Chaing, A transient three-dimensional inverse geometry problem in estimating the space and time-dependent irregular boundary shapes, *International Journal of Heat and Mass Transfer* 51 (2008) 5238–5246.
- [35] M. Dal, *Modélisation magnéto-thermohydraulique d'une pièce soumise à un procédé de soudage tig et estimation d'évolution d'un front de fusion* (Ph.D. thesis), Université de Bretagne-Sud, 2011.
- [36] P. Le Masson, M. Dal, *Analysis of Errors in Measurements and Inversion, Thermal Measurements and Inverse Techniques*, CRC Press, Taylor and Francis, 2010 (Chapter 16).